Effects of Temporal Sampling Interval on the Moon-Based Earth Observation Geometry

Hanlin Ye [ID], Wei Zheng [ID], Huadong Guo [ID], *Member, IEEE*, and Guang Liu [ID], *Member, IEEE*

Abstract—The effects of temporal sampling interval on the moon-based earth observation geometry are analyzed in this study based on three observation angles, namely viewing zenith angle, solar zenith angle, and relative azimuth angle. According to the definitions of these three angles, the calculation method for these angles and their variations between adjacent temporal samplings are deduced. Furthermore, the effects of the different positions of the lunar surface on the observation angles are derived. The results show that the variations of the nadir point and subsolar point determine the variations of the viewing zenith angle and solar zenith angle, respectively, whereas the relative azimuth angle needs to consider the relative variations of the moon-based platform's nadir point and the subsolar point. By evaluating the variations of these three observation angles, it is found that the effects of the temporal sampling interval will have significant impacts on the relative azimuth angle of the observed points at mid-low latitude regions, especially near the regions of the moon-based platform's nadir point and the subsolar point. In conclusion, the observation angles can characterize the moon-based earth observation geometry, and enlarging the temporal sampling interval will lead to the obvious impacts on the observation geometry in the mid-low latitude regions, especially the loss of the sampling of the relative azimuth angle.

Index Terms—Moon-based earth observation platform, observation angles, observation geometry, temporal sampling interval.

I. INTRODUCTION

MANY countries and international organizations became interested in the development of lunar bases [1]–[4]. When a lunar base is finally established on moon, it will be used in many aspects. A moon-based earth observation platform is one of them [5].

Observing the earth from the lunar surface can be dated back to 1970s during the Apollo 16 mission [6]. The astronauts deployed a far-ultraviolet camera on the lunar surface and terrestrial atmosphere and the geocorona was observed [7]. As an earth observation platform, the moon-based platform offers particularities, relative to existing space-borne and air-borne earth observation platforms, in that it allows a long lifetime, whole disk view, and unique perspective observation of the earth moon-facing hemisphere [5]. Thus, it is possible to observe large-scale geoscience phenomena that have not yet to be solved by existing earth observation platforms.

To utilize a moon-based earth observation platform, it is necessary to study the moon-based earth observation geometry. Some pioneer research works have been done. The studies can be roughly divided into two categories.

The first category is the construction of the observation geometry and the effects of factors on the observations. The most basic method to establish observation geometry is to unify the coordinates of moon-based platform's position and observation target's position into the same reference system. Then, the basic model can further be improved according to the specific sensors. Guo *et al.* [5] studied the observation geometry and proposed scientific concept and potential applications of moon-based earth observations. Johnson *et al.* [8] analyzed the observation geometry of a moon-based platform and discussed the advantages and constraints of the observations. Moccia and Renga [9] studied the observation geometry of synthetic aperture radar (SAR). Fornaro *et al.* [10] used a simplified Keplerian six-parameter moon orbital model to develop the observation geometry of SAR. Xu *et al.* [11]–[13] revealed the effects of earth's curvature, lunar revolution, and earth's irregular rotation on the image performance of a moon-based SAR by analyzing the observation geometry.

The idea of the second category is the analysis of observation geometric parameters calculated by the proposed model. The core of these achievements is to attempt to make suggestions to some important issues concerning the establishment of the moon-based platform by analyzing the observation geometric parameters. According to the analysis of spatio-temporal coverage, the site selection issue of a moon-based platform is discussed. Ren *et al.* [14] proposed a moon-based earth observation simulation system and evaluated the observation performance of equipping sensors at different positions on the lunar surface. Ye *et al.* [15], [16] analyzed the spatio-temporal coverage by means of the numerical simulation so as to give suggestions to

the site selection issue. Song *et al.* [17] calculated the earth's outgoing radiation at the near side of the moon by using the moon-based earth observation geometric model. Ye *et al.* [18] evaluated the effects of platform's position errors on geolocation for a sensor and suggested that equipping sensors on the mid-high region will have less effects than that on other regions. Dong *et al.* [19] presented the calculation of spatio-temporal baseline and effective spatial coverage of moon-based SAR repeat-track interferometry according to the description of observation geometry. By analyzing the line-of-sight vector error, the suggested spatial resolution of a moon-based platform can be given. Ye *et al.* [20] analyzed the pointing error of line-of-sight vector. Guo *et al.* [21] revealed the relationship between the geolocation error and exterior orientation elements' error, giving guidance to spatial resolution selection.

In addition to spatio-temporal coverage and line-of-sight vector, the effects of the temporal sampling interval on the observation geometry are also worth studying. To achieve this goal, the main idea is to propose a set of indicators to characterize the observation geometry first, and then, reveals its relationship of the variations to the temporal sampling interval. In this study, the observation angles including the solar zenith angle, viewing zenith angle, and relative azimuth angle are selected to characterize the observation geometry for the observed point directly. The observation angles are important parameters in earth observation. In the field of atmospheric science, the view zenith angle is the main parameter to retrieval of the atmospheric composition, such as the total ozone column [22], [23]. In oceanography, observation angle will affect the retrieval accuracy of ocean color and other related parameters [24], [25]. Besides, the observation angle also plays an important role in the field of earth's radiation budget. The observation angular anisotropy must be considered when transforming the measured radiance at a single angle to the inferred hemispheric flux of leaving element [26], [27]. Thus, the multiangular observations are helpful in characterizing a variety of earth parameters. To investigate these parameters, Guo *et al.* [28] presented the observation angular characteristics of a moon-based platform. Pallé and Goode [29] discussed the possibility of earth's radiation budget monitoring from the view of observation angular sampling. These studies have provided valuable insights for the observation angles.

However, there are few studies concerning about the observation angles and its relationship to the temporal sampling interval. The observation angles for a moon-based platform has distinct features. A moon-based platform can observe almost the whole hemisphere of the earth, and the variation observation angles for every position in the observational scope are contiguous. For each observed point, different positions have different variation characteristics of observation angles. Another important issue is the effects of temporal sampling interval on the observation angles, which is also quite different from the case of existing space-borne platforms. Large observation scope will include more information. A moon-based platform provides finite sampling interval observations, which essentially is the sampling of the observation angles. Different temporal sampling intervals will lead to different sampling of the observation angles of the observed points at different latitudes. Larger temporal sampling interval will lead to the loss of the observation angles.

Therefore, it is necessary to analyze the effects of different temporal sampling intervals on the observation angles and understand its impacts on the observation geometry.

Different from the previous studies, this study investigates the variations of the observation angles and their relationship to the temporal sampling interval. This research makes three contributions. The first is to express the moon-based earth observation geometry by three observation angles. The definition and relevant calculations of these observation angles are presented in this study. Different from [28], which includes four parameters, we reduce the solar azimuth angle and view azimuth angle to the relative azimuth angle (i.e., the difference of above two) and deduce theoretical expression. The second contribution is to parameterize the observation angles and reveals the relationships between observation angles of observed point and nadir point's position. This enabled us to characterize the spatio-temporal distribution of observation angles and their variations relative to the cases of the nadir point without heavy point-to-point calculations. Third, the effects of temporal sampling interval on these three observation angles are revealed respectively finally.

II. MOON-BASED EARTH OBSERVATION GEOMETRIC MODEL

The regular method of studying moon-based earth observation geometric characteristics is to establish a moon-based earth observation geometric model, and this requires parameterization of the observation geometry, which are essentially the positions of the moon-based platform and the points on earth. In this section, since this study mainly focuses on the effects of temporal sampling intervals on the observation geometry, the earth's topography and the atmospheric refraction are not considered in this model.

A general earth observation geometric model typically starts with the orbital and attitude information of the platform [14], [20]. The sensor's position and attitude are usually defined in the geocentric celestial reference system (GCRS), which is an inertial reference system, whereas the positions on earth are defined in the geodetic reference system. Through a series transformation, the sensor's position and the positions on earth are unified into the same reference system, i.e., the International Terrestrial Reference System (ITRS). However, in the moon-based earth observations, the geometric model is quite different. The moon is a natural celestial body. Sensors can be equipped anywhere on the lunar surface where the earth is visible. This leads to the fact that the position of a sensor cannot be simplified as at the barycenter of the moon, but on the surface of the moon. It is just because of this distinction that makes the reference system transformations involved in the geometric model more complex. The determination of the platform's position relies on the astrometric theory. Furthermore, the precise descriptions of the attitude of the moon and earth orientation need to be considered due to the extremely long earth–moon distance.

In the moon-based earth observation geometric model, six main reference systems are involved, including International Celestial Reference System (ICRS), GCRS, Selenocentric Celestial Reference System (SCRS), Moon-Centered Moon-Fixed Reference System, and ITRS. Fig. 1 summarizes the general
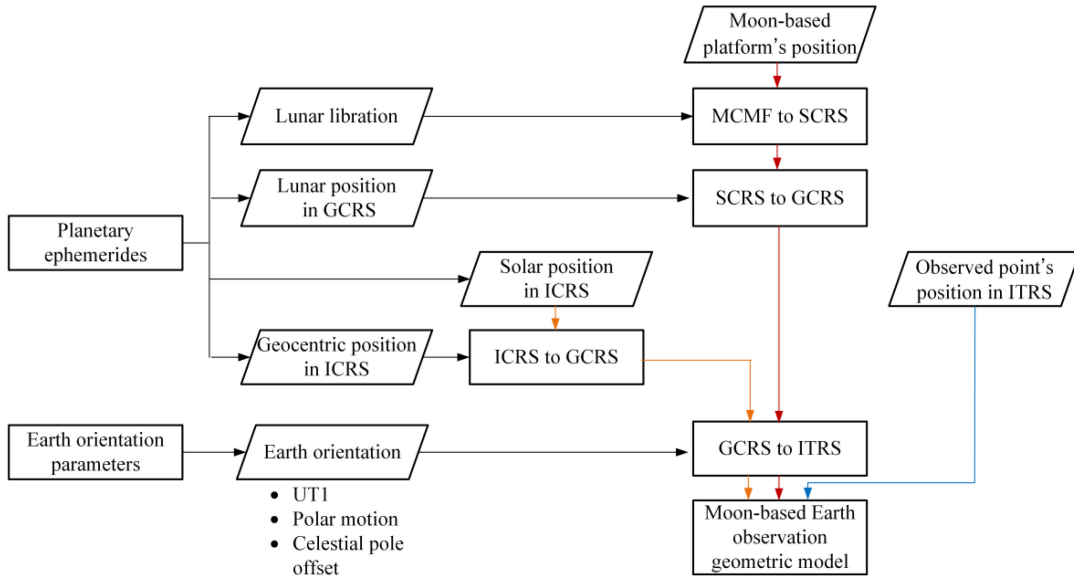
Fig. 1. General procedures of the moon-based earth observation geometric model.

procedures of the geometric model, including the required orbit and attitude data and the detailed coordinate transformations.

The planetary ephemerides can be utilized to provide the positions and attitude of the moon. There are some planetary ephemerides published by different organizations [30]–[32]. The development ephemeris (DE) established by the Jet Propulsion Laboratory is one of the widely used ephemeris in the world and is available via World Wide Web.[1] There are many versions of this ephemeris, which are designated DEs (followed by a number). We selected DE430 due to the improvements for the orbit and attitude of the moon through use of additional Lunar laser ranging data and improved lunar gravity field [33]. The ephemeris DE430 is expressed in coordinates referred to the International Celestial Reference Frame 2 (ICRF2), which is an updated reference frame of ICRF. The ICRF2 is the realization of the ICRS. The origin of the ICRS is the barycenter of the solar system, with the principle plane (i.e., *XY* plane) close to the mean equator of J2000.0 [34]. There is a small shift between the J2000.0 inertial reference system and ICRS, which can be transformed by a constant matrix [35]. The corresponding time system of DE430 is the Barycentric Dynamical Time (TDB) [33]. For the lunar position, the coordinates derived from DE430 are tabulated as the origin at the earth barycenter, i.e., the GCRS. As regard to the attitude of the moon, it is parameterized by Euler angles derived from DE430 [36], [37].

Earth's rotation is not even. We utilized the earth orientation parameters (EOP) to describe the rotation irregularities all together. There are five parameters in the EOPs including universal time (UT1), coordinates of the pole (i.e., the two parameters of polar motion), and the celestial pole offset (two parameters relative to the IAU Precession and Nutation models) [35], [38]. These five parameters associated with other relative parameters provide the transformation matrices between the

ITRS and GCRS as a function of time. The EOP can be downloaded from the website.[2]

The coordinate transformations have three important components, which includes the sun, earth, and moon. All the transformation processes aim to transform the position of the sun and the moon-based platform into a unified reference system at a specific time. For convenient calculation of the observation angle, we transformed the positions into the ITRS. The ITRS is an earth-centered rotating reference system that is suitable for describing the earth's surface. Its *z*-axis aligning with the conventional international origin pole and the *x*-axis passes through the intersection of the equatorial plane and the prime meridian [35].

For the calculation of the moon-based platform's position, the procedure is to transform the moon-based platform's position into the ITRS. The original position is defined as longitude λ_m, latitude φ_m, and altitude h_m. The transformation is a six-step process. Assuming the moon to be a sphere, the counterparts of the moon-based platform's position in the ITRS are obtained by following transformation [16], [20]:

$$\boldsymbol{p}_{\mathrm{ITRS}} = [\boldsymbol{\Pi}][\Theta][\mathbf{N}][\mathbf{P}][\mathbf{B}][\mathbf{M}][\mathbf{L}][\mathbf{C}]$$

$$\begin{bmatrix} (R_\mathrm{m} + h_m)\cos(\varphi_m)\cos(\lambda_\mathrm{m}) \\ (R_m + h_m)\cos(\varphi_m)\sin(\lambda_\mathrm{m}) \\ (R_m + h_m)\sin(\varphi_\mathrm{m}) \end{bmatrix} \quad (1)$$

where R_m is the radius of the moon. [$\mathbf{C}$], [$\mathbf{L}$], [$\mathbf{M}$], [$\mathbf{P}$], [$\mathbf{N}$], [Θ], [$\boldsymbol{\Pi}$], and [$\mathbf{B}$] represent, respectively, constant, lunar libration, offset of the origin from the SCRS to the GCRS, precession, nutation, rotation, polar motion, and bias matrix [16].

For the calculation of the solar position, two transformations need to be gone through. The first is to transform the coordinates

---

[1][Online]. Available: ftp://ssd.jpl.nasa.gov/pub/eph/planets/.

[2][Online]. Available: ftp://hpiers.obspm.fr/iers/.

to GCRS. Then, the position in the ITRS can be calculated by the transformation matrixes between the GCRS and ITRS. The transformations can be expressed as

$$s_{\mathrm{ITRS}} = [\mathbf{\Pi}][\mathbf{\Theta}][\mathbf{N}][\mathbf{P}][\mathbf{B}][\mathbf{G}]s_{\mathrm{ICRS}} \qquad (2)$$

where $[\mathbf{G}]$ represents the offset matrix of the origin from the barycenter of the solar system and the earth.

Through a series of transformations, the positions of the sun and the moon-based platform are finally unified in the ITRS, and the earth observation geometry is shown. There are some features of this earth observation geometry. First and obviously, since the distance between the earth and the moon is very large and observing the earth only need 2° field angle viewing from the moon, the observational scope is similar to a spherical cap, which almost covers the hemisphere of the earth. However, both the spherical cap and the earth scene in the observational scope are not constant. The changing lunar position determines the earth scene and the elliptical orbit of the moon leads to the periodical changing size of the "spherical cap." For the orbit of the moon, it takes the moon about 27.3 days (27 days, 7 h, 43 min) to complete the cycle. When considering the relationship to the sun, the earth being around, half of it is lit up by the sun. The side that the moon-based platform can observe is with partial illumination. As the moon goes around the earth, the portion of the sunlit part will have cyclic variation. The variation cycle is about 29.5 days (29 days, 12 h, 44 min). The observations of the point in the observational scope are continuous regardless of its coordinates. This makes it possible to reduce the sampling interval, while at the same time considering the observation angular coverage. Another important feature is the changing orbital inclination, leading to the changing observation angle for the certain position on earth. Maximum orbital inclination relative to the earth equator varies between 28° and –28° during every 18.6 years, whereas the minimum ranges from 18° to–18° about 9.3 years later [21]. Such orbital inclination is enough to cover the total Arctic or Antarctic region during one orbital period. Furthermore, changing orbit of the moon can bring much wider variety of observation angles.

III. THEORETICAL MODEL FOR OBSERVATION GEOMETRY

For an observed point on earth, the moon-based earth observation geometry can be characterized through three observation angles, called the solar zenith angle, the viewing zenith angle, and the relative azimuth angle. In this section, we first defined these three observation angles in the topocentric reference system. Then, the calculation methods for the observation angles are introduced according to the definitions. Furthermore, to be more serious, the effects of the different positions of the lunar surface on the observation angles are derived.

A. Observation Angular Definition and Calculation

According to the geometric model, the moon-based platform's position, the solar position, and the earth are in the same reference system. To calculate the observation angles, we introduced a new reference system named topocentric reference system. It is a Cartesian reference system that is tangent to the earth
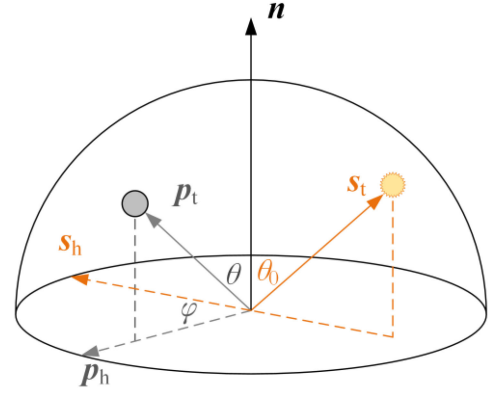

Fig. 2. Schematic of the observation angles.

surface at an observed point with its fundamental plane is the local horizon. The north axis points to the north direction and the zenith axis is perpendicular to the fundamental plane. This reference system conveniently divides the sky into the upper hemisphere that the sensor can observe. Viewing zenith angle θ in Fig. 2 is the angle between the local zenith (i.e., directly above the observed point and perpendicular to the horizontal plane) and the line of sight from the moon-based platform's sensor to that point. Solar direction is an important factor in the observation geometry. Solar zenith angle θ_0 in Fig. 2 is the angle between the local zenith and the solar direction. Previous studies decomposed the solar direction of an observed position into two parameters, i.e., solar azimuth angle and solar zenith angle [28]. In this study, the relative azimuth angle φ is proposed to characterize the relationship between the solar azimuth angle and viewing azimuth angle. As shown in Fig. 2, solar plane is formed by the solar direction and its projection direction on the horizontal plane of the observed position. Based on such plane, the relative azimuth angle can be defined. The relative azimuth angle is defined as the viewing azimuth angle direction relative to the solar plane, which is in the range of 0°–180°. In brief, the relative azimuth angle is the absolute difference between the viewing azimuth angle and solar azimuth angle. The forward reflection of sunlight corresponds to 0°, and backward reflection corresponds to 180°. The definition of the relative azimuth angle connects the sun and the moon-based platform in the azimuth angle, which can reveal the variation regularity of the sunlit portion in the observational scope.

The line-of-sight vector and solar direction vector in the topocentric reference system need to be calculated first. Based on this reference system, solar zenith angle, viewing zenith angle, and relative azimuth angle are calculated separately.

The observation angles describe the line-of-sight in the topocentric reference system. Thus, to unify the reference system, $[\mathbf{R}]$ is defined to describe the transformations from the ITRS to the topocentric reference system, i.e.,

$$[\mathbf{R}] = \begin{pmatrix} -\sin\varphi_{\mathrm{d}} & \cos\varphi_{\mathrm{d}} & 0 \\ -\cos\varphi_{\mathrm{d}}\sin\theta_{\mathrm{d}} & -\sin\varphi_{\mathrm{d}}\sin\theta_{\mathrm{d}} & \cos\theta_{\mathrm{d}} \\ \cos\varphi_{\mathrm{d}}\cos\theta_{\mathrm{d}} & \sin\varphi_{\mathrm{d}}\cos\theta_{\mathrm{d}} & \sin\theta_{\mathrm{d}} \end{pmatrix} \qquad (3)$$

where φ_d and θ_d is the longitude and colatitude of the observed point's position.

Given the line-of-sight vector in the ITRS p_0, its counterpart in the topocentric reference system p_t can be calculated as

$$p_t = [\mathbf{R}]p_0. \tag{4}$$

Similar to the case of line-of-sight vector, the transformation process from solar direction in the ITRS s_0 to the topocentric reference system s_t can be given by

$$s_t = [\mathbf{R}]s_0. \tag{5}$$

Thus, the viewing zenith angle can be expressed as

$$\theta = arccos\left(\frac{p_t \cdot n}{|p_t|\,|n|}\right). \tag{6}$$

The solar zenith angle can be written as

$$\theta_0 = arccos\left(\frac{s_t \cdot n}{|s_t|\,|n|}\right) \tag{7}$$

where n is the normal vector of the horizontal plane.

The calculation of the relative azimuth angle will be more complex due to the considerations of the solar direction. According to the coordinate of the moon-based platform and the sun, we defined the projection of the moon-based platform and the sun on the horizontal plane as p_h and s_h, respectively. The relative azimuth angle can be calculated as

$$\varphi = 2\pi - arccos\left(\frac{p_h \cdot s_h}{|p_h|\,|s_h|}\right). \tag{8}$$

B. Effects of Different Positions at Lunar Surface on the Observation Angles

Since the moon is a celestial body, equipping sensors on different positions of the lunar surface will have different sight conditions to the earth [15], [16]. In the permanent earth observation region (80°W–80°E and 81°S–81°N), there will also be some differences. In this section, the impacts of equipping sensors at different positions on the observation angles are derived.

To reveal the differences, we calculated the angular differences between the line-of-sight vector from the observed point to the moon-based platform's position and the vector from the observed point to the lunar position.

Given the lunar coordinates x_m, y_m, and z_m and the observed point's coordinates x_e, y_e, and z_e, the vector to the observed point's position is

$$\mathbf{m} = \begin{pmatrix} x_m - x_e \\ y_m - y_e \\ z_m - z_e \end{pmatrix}. \tag{9}$$

Denoting the moon-based platform's coordinates x_b, y_b, and z_b, the line-of-sight vector $\mathbf{p}_0$ can be expressed as

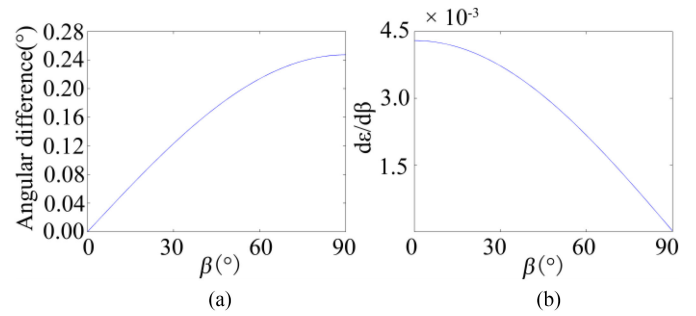$$\mathbf{p}_0 = \begin{pmatrix} x_b - x_e \\ y_b - y_e \\ z_b - z_e \end{pmatrix}. \tag{10}$$

Fig. 3.   (a) Variation of the observation angular difference. (b) Deviation of the observation angular difference.

Thus, the angular difference can be calculated as

$$\varepsilon = arccos\left(\frac{\mathbf{m} \cdot \mathbf{p}_0}{|\mathbf{m}|\,|\mathbf{p}_0|}\right). \tag{11}$$

Equation (11) shows that the magnitude of the angular differences depends on the vector $\mathbf{p}_0$, whereas the vector $\mathbf{p}_0$ is subject to the position on the lunar surface

$$\mathbf{p}_0 = \mathbf{m} + \mathbf{d}_0 \tag{12}$$

where $\mathbf{d}_0$ is the vector from lunar position to the position on the lunar surface.

With the given $\mathbf{p}_0$ above, the angular difference in (11) can now be rewritten as

$$\varepsilon = arccos\left(\frac{\mathbf{m} \cdot (\mathbf{m} + \mathbf{d}_0)}{|\mathbf{m}|\,|\mathbf{m} + \mathbf{d}_0|}\right). \tag{13}$$

Applying the principle of vector calculation to obtain the relation of the angle β between the vector $\mathbf{m}$ and vector $\mathbf{d}$, the angle ε in (13) becomes

$$\varepsilon = arccos\left(\frac{|\mathbf{m}| + \cos\beta\,|\mathbf{d}_0|}{\sqrt{|\mathbf{m}|^2 + 2\,|\mathbf{m}|\,|\mathbf{d}_0|\cos\beta + |\mathbf{d}_0|^2}}\right). \tag{14}$$

It is worth noting that the domain of angle β is [0 90°]. According to (14), the maximum angular difference can be calculated.

Taking the derivative of (14), the expression can be written as

$$\frac{d\varepsilon}{d\beta} = \frac{|\mathbf{m}|\,|\mathbf{d}_0|\cos\beta + |\mathbf{d}_0|^2}{|\mathbf{m}|^2 + 2\,|\mathbf{m}|\,|\mathbf{d}_0|\cos\beta + |\mathbf{d}_0|^2}. \tag{15}$$

In Fig. 3, we first illustrated the observation angular differences with changing moon-based platform's position. It is clear that the observation angular difference is related to the angle between the moon-based platform's position vector and the lunar position vector observed from the point on earth. With the angle β increasing, the observation angular difference varies from 0° to 0.245°, showing a very small difference. In conjunction with Fig. 3(b), it is found that the largest difference is shown at 90°. That means, the maximum observation angular difference will occur in the limb of the lunar disk where the line-of-sight vector is tangent to the lunar surface. As for the angle β variation during one orbital period, it is substantially affected by the distance. The shorter the distance between the point on earth
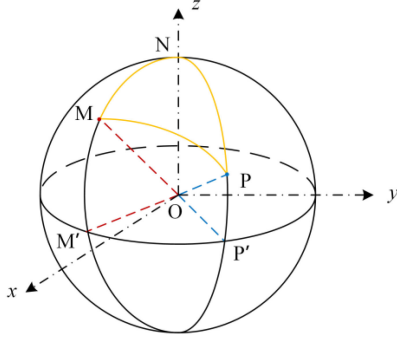
Fig. 4. Illustration of the observed point (P) and the moon-based platform (M) on the sphere. N is the North Pole. M' and P' are the projections of M and P on the earth equator.

and the moon-based platform, the greater maximum angle β is. According to the shortest distance, the greater maximum observation angular difference β is about 0.26°.

IV. CALCULATION METHOD FOR OBSERVATION GEOMETRIC DIFFERENCES BETWEEN ADJACENT TEMPORAL SAMPLINGS

For the moon-based earth observations, the observation angles reflect the current observation geometry of the observed point. In an ideal condition, a moon-based sensor can observe the earth all the time, and all the observations will be recorded. However, in actual condition, the observations will be sampled at a certain temporal sampling interval. As the temporal sampling interval becomes coarser, the observations will be sampled sparsely, as reflected in the samplings of these three observation angles. In this section, based upon the relationship to the nadir point, the variations of the observation angles are investigated. Then, the observation angular differences between adjacent temporal samplings are deduced by taking the direction derivative of the observation angles at the direction of the nadir point's movement.

A. Relationship Between Observation Angles of Observed Point and Nadir Point's Position

The observation angles for an observed point are related to that in the nadir point, which can be calculated by deducing the relationship of the observation angles between the nadir point and the observed points. The nadir point changes over time. With the nadir point changing, the variations of the observation angles can be derived.

The observation angles defined in previous section are mainly divided into zenith angle and azimuth angle. The zenith angle, including solar zenith angle and the viewing zenith angle, is the angle based on the normal vector, whereas the azimuth angle, i.e., the relative azimuth angle, is the angle projected on the horizontal plane. Therefore, in this section, the relationship is revealed from the aspect of the zenith angle and the azimuth angle for the sake of simplicity.

As shown in Fig. 4, denoting the point O is the earth's barycenter, and the point N is the North Pole. The point M indicates the nadir point, and the point P represents the observed

point's position. The goal is to derive the relationship between the observed point and the nadir point by using spherical triangle cosine theorem.

The first step is to calculate the nadir point. Given the positions x_b, y_b, and z_b in the ITRS, the nadir point, including latitude, longitude, and altitude, can be calculated as [39]

$$
\begin{cases}
\lambda_b = \arctan(\frac{y_b}{x_b}) \\
\varphi_b = \arctan(\frac{z_b(N+H)}{\sqrt{(x_b^2+y_b^2)[N(1-e^2)+H]}}) \\
H = \frac{Z}{\sin(\varphi_b)} - N(1-e^2)
\end{cases} \quad (16)
$$

The azimuth angle and zenith angle of the observed point can be expressed in terms of the angles and sides of the spherical triangle MPN. Referring to Fig. 4, the zenith angle is the complement of the central angle of arc MP, whereas the azimuth angle is the angle MPN.

By using the cosine formula, we have

$$
\cos\left(\theta_v\right) = \cos\left(\frac{\pi}{2} - \theta_b\right)\cos\left(\frac{\pi}{2} - \theta_d\right) \\
+ \sin\left(\frac{\pi}{2} - \theta_b\right)\sin\left(\frac{\pi}{2} - \theta_d\right)\cos\left(\varphi_b - \varphi_d\right). \quad (17)
$$

The zenith angle θ_v can be written as

$$
\theta_v = \arccos(\sin(\theta_b)\sin(\theta_d) \\
+ \cos(\theta_b)\cos(\theta_d)\cos(\varphi_b - \varphi_d)). \quad (18)
$$

Substituting zenith angle θ_v, by using the cosine formula

$$
\cos\left(\frac{\pi}{2} - \theta_b\right) = \cos\left(\frac{\pi}{2} - \theta_d\right)\cos(\theta_v) \\
+ \sin\left(\frac{\pi}{2} - \theta_d\right)\sin(\theta_v)\cos(\varphi_v). \quad (19)
$$

The azimuth angle can be expressed as

$$
\varphi_v = \arccos\frac{\sin(\theta_b) - \sin(\theta_d)\sin(\theta_v)}{\cos(\theta_d)\cos(\theta_v)}. \quad (20)
$$

B. Observation Angular Differences Between Adjacent Temporal Samplings

The limited temporal sampling interval will constrain the sampling of the observations, thus affecting the sampling of the observation angles. In such condition, a question arises to pose as: how much differences of the observed angles are between the adjacent temporal samplings? The variation of the observation angles of the observed point can be described as the nadir point's position and observed point's position. Thus, this question can be answered by taking the direction derivative of the observation angles at the direction of the nadir point's movement.

Substituting the moon-based platform's nadir point (φ_p, θ_p) into (φ_b, θ_b) in (17), the differences of the viewing zenith angles at adjacent temporal samplings can be approximated by the directional derivative of (17)

$$
\Delta\theta = \frac{\partial\theta}{\partial\theta_p}\sin(\alpha) + \frac{\partial\theta}{\partial\varphi_p}\cos(\alpha) \quad (21)
$$

where α is the angle between the latitudinal and the movement direction of the moon-based platform, $\partial\theta/\partial\theta_p$ and $\partial\theta/\partial\varphi_p$ are

the partial derivatives with respect to the latitudinal and longitudinal direction of the nadir point, respectively, with expressions of

$$\frac{\partial \theta}{\partial \theta_p} = \frac{-\sin(\theta_d)\cos(\theta_p) + \sin(\theta_p)\cos(\theta_d)\cos(\varphi_p - \varphi_d)}{\sin \theta} \tag{22}$$

$$\frac{\partial \theta}{\partial \varphi_p} = \frac{\cos(\theta_p)\cos(\theta_d)\cos(\varphi_p - \varphi_d)}{\sin \theta}. \tag{23}$$

Similar to the case of viewing zenith angle, the differences of solar zenith angles at adjacent temporal samplings only need to substitute the moon-based platform's nadir point to the subsolar point in (21)–(23), given the subsolar point (φ_s, θ_s), the expression can be written as

$$\Delta \theta_0 = \frac{\partial \theta_0}{\partial \theta_s}\sin(\alpha_s) + \frac{\partial \theta_0}{\partial \varphi_s}\cos(\alpha_s) \tag{24}$$

where α_s is the angle between the latitudinal and the movement direction of the sun, and $\partial \theta_0/\partial \theta_s$ and $\partial \theta_0/\partial \varphi_s$ are given by

$$\frac{\partial \theta_0}{\partial \theta_s} = \frac{-\sin(\theta_d)\cos(\theta_s) + \sin(\theta_s)\cos(\theta_d)\cos(\varphi_s - \varphi_d)}{\sin \theta_0} \tag{25}$$

$$\frac{\partial \theta_0}{\partial \varphi_s} = \frac{\cos(\theta_s)\cos(\theta_d)\cos(\varphi_s - \varphi_d)}{\sin \theta_0}. \tag{26}$$

For the case of relative azimuth angle, according to its definition, the value of the relative azimuth angle is subjected to both the moon-based platform's nadir point and the subsolar point. The difference between adjacent temporal samplings is essentially the sum of the change of the azimuth angle caused by the movement of the moon-based platform $\Delta \varphi_m$ and the sun $\Delta \varphi_s$. Thus, we write the expression according to the definition

$$\Delta \varphi = \Delta \varphi_m + \Delta \varphi_s$$

$$= \frac{\partial \varphi_m}{\partial \theta_p}\sin(\alpha) + \frac{\partial \varphi_m}{\partial \varphi_p}\cos(\alpha)$$

$$+ \frac{\partial \varphi_0}{\partial \theta_s}\sin(\alpha_s) + \frac{\partial \varphi_0}{\partial \varphi_s}\sin(\alpha_s). \tag{27}$$

Among them, $\partial \varphi_m/\partial \varphi_p$, $\partial \varphi_m/\partial \varphi_p$, $\partial \varphi_0/\partial \varphi_s$, and $\partial \varphi_0/\partial \varphi_s$ can be written as

$$\frac{\partial \varphi_m}{\partial \theta_p} =$$

$$\frac{\cos(\theta_p) - \sin(\theta_d)\cos(\theta)\frac{\partial \theta}{\partial \theta_p} + [\sin(\theta_p) - \sin(\theta_d)\sin(\theta)]\tan(\theta)\frac{\partial \theta}{\partial \theta_p}}{-\sqrt{[\sin(\theta_p) + \cos(\theta_d + \theta)][\cos(\theta_d - \theta) - \sin(\theta_p)]}} \tag{28}$$

$$\frac{\partial \varphi_m}{\partial \varphi_p} =$$

$$\frac{-\sin(\theta_d)\cos(\theta)\frac{\partial \theta}{\partial \varphi_p} + [\sin(\theta_p) - \sin(\theta_d)\sin(\theta)]\tan(\theta)\frac{\partial \theta}{\partial \varphi_p}}{-\sqrt{[\sin(\theta_p) + \cos(\theta_d + \theta)][\cos(\theta_d - \theta) - \sin(\theta_p)]}} \tag{29}$$

$$\frac{\partial \varphi_0}{\partial \theta_s} =$$

$$\frac{\cos(\theta_s) - \sin(\theta_d)\cos(\theta_0)\frac{\partial \theta_0}{\partial \theta_s} + [\sin(\theta_s) - \sin(\theta_d)\sin(\theta_0)]\tan(\theta_0)\frac{\partial \theta_0}{\partial \theta_s}}{-\sqrt{[\sin(\theta_s) + \cos(\theta_d + \theta_m)][\cos(\theta_d - \theta_m) - \sin(\theta_s)]}} \tag{30}$$

$$\frac{\partial \varphi_0}{\partial \varphi_s} =$$

$$\frac{-\sin(\theta_d)\cos(\theta_0)\frac{\partial \theta_0}{\partial \varphi_s} + [\sin(\theta_s) - \sin(\theta_d)\sin(\theta_0)]\tan(\theta_0)\frac{\partial \theta_0}{\partial \varphi_{\backslash s}}}{-\sqrt{[\sin(\theta_s) + \cos(\theta_d + \theta_0)][\cos(\theta_d - \theta_0) - \sin(\theta_s)]}}. \tag{31}$$

By deducing the observation angular differences between adjacent temporal samplings, it is clear that the differences of the viewing zenith angle and solar zenith angle are subjected to the nadir point and subsolar point, respectively, whereas the differences of the relative azimuth angles are dependent on the interaction of the nadir point and subsolar point.

V. RESULTS AND DISCUSSIONS

The theoretical framework for observation geometry was introduced in Sections III and IV. Here, experiments are set up to analyze the spatio-temporal variation of the observation angles and observation angular differences with regard to the sampling interval. Finally, the observation angular differences caused by different sampling intervals are discussed.

A. Spatio-Temporal Variation Analysis of the Observation Angles

In Section III, it is demonstrated that equipping sensors on the different positions of the lunar surface lead to no significant difference in the analysis of observation angles. Thus, we assumed that the moon-based platform was located at the center of the lunar disk, i.e., the selenographic coordinates of (0°N, 0°E).

Fig. 5 illustrates the distribution and daily variation of the viewing zenith angle. As expected, the distribution of the viewing zenith angle presents concentric circle diffusion, ranging from 90° to 0°. The nadir point has an important impact on the viewing zenith angular distribution. The maximum value will be shown in the nadir point of the moon-based platform. The daily variation of viewing zenith angle changes with the nadir point continuously. The effect of nadir point becomes even more critical in the variation of orbital period. Since the nadir point of a moon-based platform can cover the latitudinal range from 28°S to 28°N, the pattern of concentric circle will move northward or southward during one orbital period. Therefore, nadir point will bring about a varied distribution of viewing zenith angle for a certain position.

In order to reveal the viewing zenith angular characteristics of the adjacent observed points, we compared the latitudinal and longitudinal variation during one orbital period. In Fig. 6(a), we calculated the viewing zenith angle of 0° longitude at different latitude. The x-axis refers to the observation time in the orbital period and the y-axis is the latitude of the 0° longitude. It is
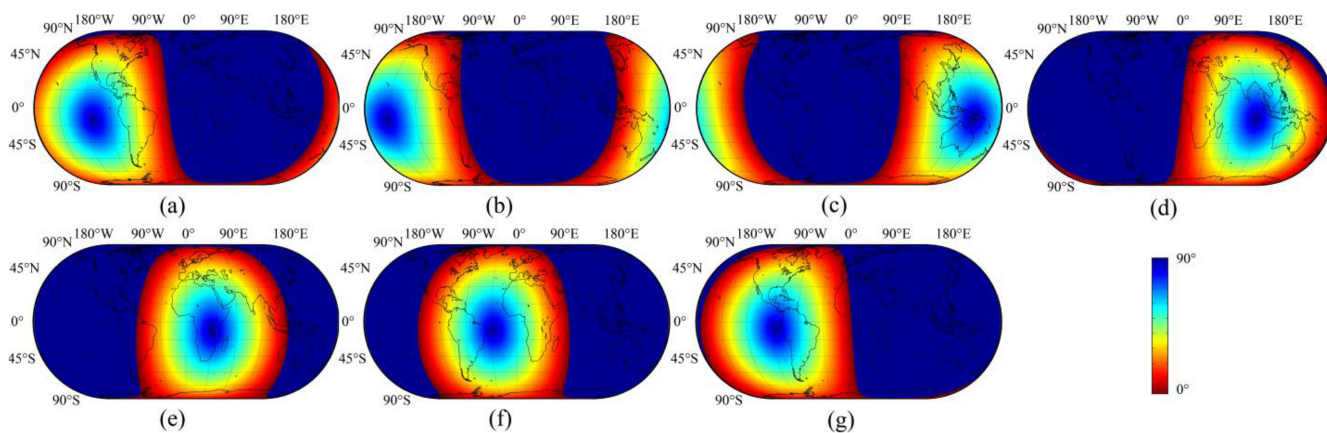
Fig. 5.   Viewing zenith angular distribution at (a) 1:00, (b) 4:00, (c) 8:00, (d) 12:00, (e) 16:00, (f) 20:00, and (g) 24:00.
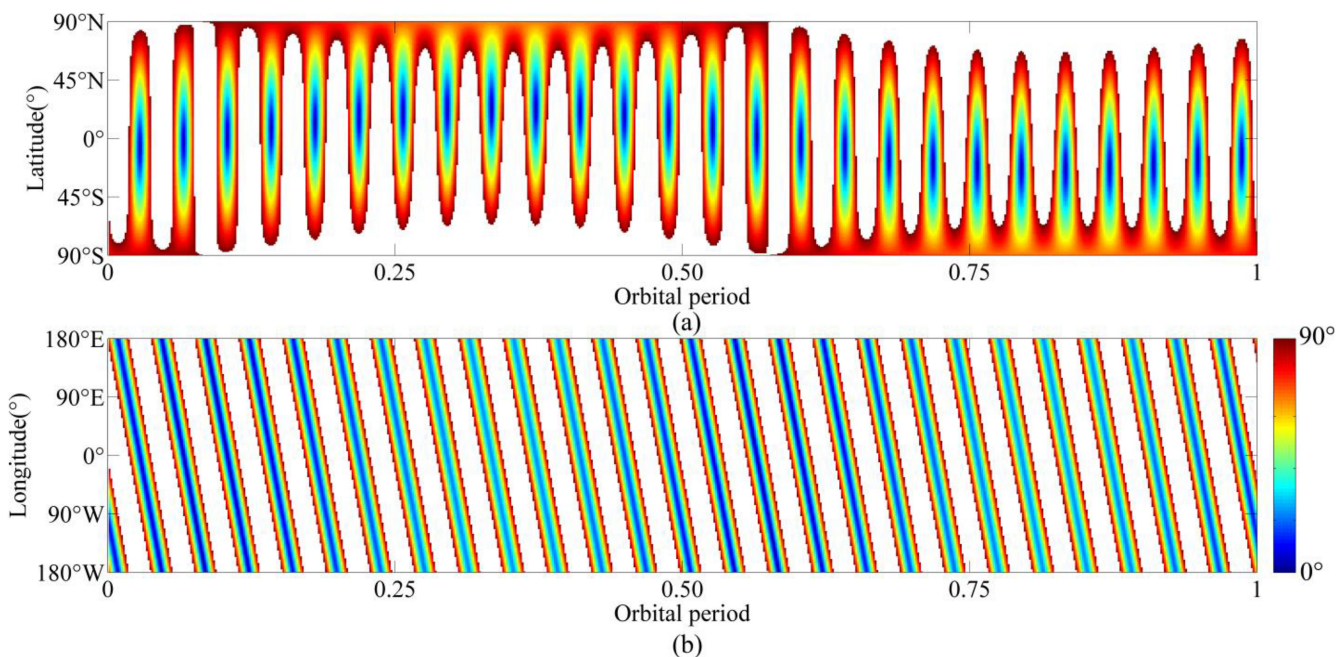

Fig. 6.   Viewing zenith angular variation along (a) latitudinal direction and (b) longitudinal direction during one orbital period.
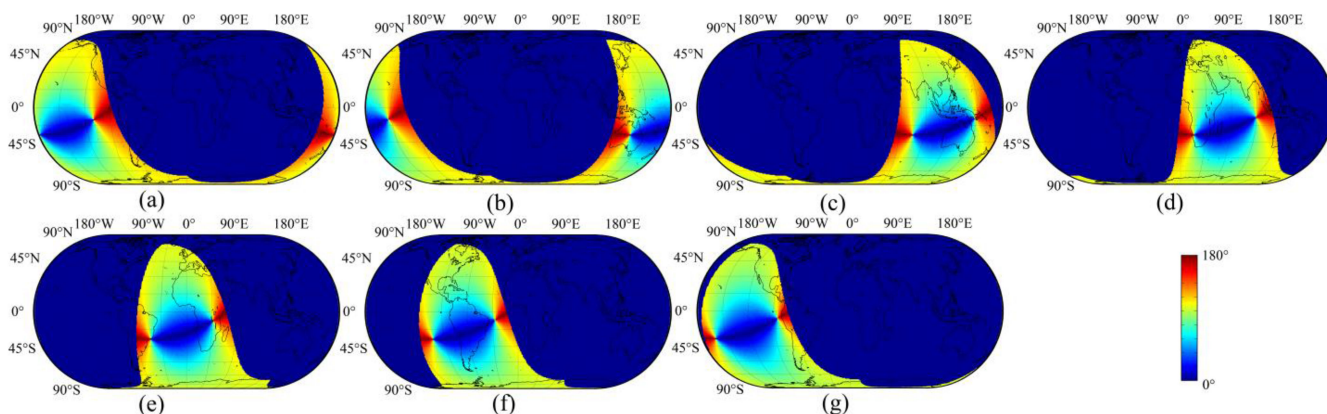

Fig. 7.   Relative azimuth angular distribution at (a) 1:00, (b) 4:00, (c) 8:00, (d) 12:00, (e) 16:00, (f) 20:00, and (g) 24:00.
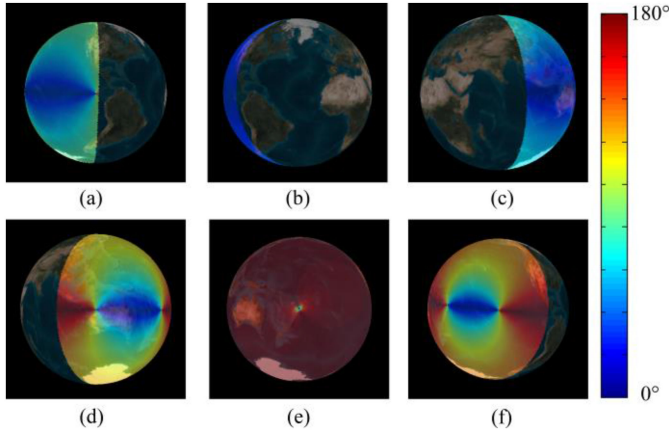
Fig. 8. Relative azimuth angular distribution on (a) January 3, (b) January 8, (c) January 16, (d) January 20, (e) January 25, and (f) January 29.

obvious that the variation at both the longitudinal direction and observation time is continuous. At mid-low latitude region of the earth, the viewing zenith angular variation ranges generally from 0° to 90°. However, such this widely variation will only be shown in the region of latitudinal range of nadir point. The variation range will be smaller with the increment of the latitude. At high latitude region, the observation time window is longer, while the variation range is significantly smaller than that at mid-low latitude region. Fig. 6(b) shows the longitudinal variation at 0° latitude of viewing zenith angle during one orbital period. Compared to Fig. 6(a), the variation is more regular, which acts as in accord with diurnal cycle. There is no significant difference between the longitudes during one diurnal cycle. Among different diurnal cycles, the viewing zenith variation range changes, which is mainly embodied in the difference of the minimum values. It appears that the variation almost covers the range from 0° to 90°. The reason is the selection of latitude to 0°. For the other latitudes, the minimum value can be referred from Fig. 6(a). For the solar zenith angle, the distribution is similar to the case of viewing zenith angle, i.e., the concentric circle pattern. The differences in the solar zenith angles is only shown in the sunlit area and with the changes of the geometric relationship between the sun and the moon.

Fig. 7 presents the distribution and daily variation of the relative azimuth angle. Different from the viewing zenith angle, the distribution of relative azimuth angle appears in the sunlit portion in the observation scope. This is because the relative azimuth angle is only defined in the sunlit area. The axis of symmetry is the line connecting the nadir point and the direct point of sunlight. According to the definition, the larger value will be shown in the forward directions to the sun and the variation of relative azimuth angle ranges from 0° to 180° generally. Since the angle between the solar position and moon-based platform's position varies relatively small during one day, there is no significant differences of the distribution in a daily cycle. However, the distributions in Fig. 8 are one of the cases of daily cycle. During one orbital period, the distribution of the relative azimuth angle can be divided into seven typical cases based

on the variation of the sunlit portion in the observation scope. Fig. 8(a)–(f) shows six distributions of the relative azimuth angle at different observation time, representing the six cases. The remaining case that has not shown in Fig. 8 is the case of no sunlit portion. With the increment of the sunlit portion, the variation range of the relative azimuth angle will be larger. When the sunlit portion covers more than 50% of the observation scope, the variation will range from 0° to 180°. At this time, the direct point of sunlight will be in the observation scope. The values in the observational scope are exactly symmetrical to the line between the direct point of the sunlight and the nadir point. When the sunlit portion covers almost all the observation scope, all the values in the observation scope are large.

We then compared the relative azimuth angle at different longitude and latitude during one orbital period. As shown in Fig. 9(a), it is obvious that the variation range is almost the same at different longitude during one day. When the direction point of sunlight is not in the observation scope, the value varies monotonically. When the sunlit portion covers most of the observation scope, the value becomes larger, whereas the variation range becomes smaller. Fig. 9(b) shows the variation along the latitudinal direction. The variation range changes with its latitude. In the mid-low latitude region, the relative azimuth angle varies continuously and the minimum value is generally as low as 0°. When the direction point of sunlight comes in the observation scope, the maximum value becomes larger until it reaches to 180°. From the view of the values in the latitudinal direction, the relative azimuth angular distribution at mid-high latitude is smaller than the case in the low latitude. In the Antarctic region in Fig. 9(b), the observation time window is about half the orbital period. The relative azimuth angle covers from 90° to 180° continuously. Note that, not all latitudinal distributions are the same at every orbital period, though all the orbital period will include a long coverage either at the Antarctic region or Arctic region. The spatial coverage of these regions is related to the latitudinal variation range of nadir point. At these positions, the relative azimuth angle is still continuous during the observation time window.

In general, the variations of viewing zenith angle and relative azimuth angle are all continuous in terms of both time and space. For the viewing zenith angle and the solar zenith angle, the range depends on the minimum value, whereas its minimum value is related to the latitude of nadir point or the subsolar point and the observed point. For the relative azimuth angle, the variation range at a certain observed point is not only subject to the sunlit portion in the observation scope, but also to its latitude. Low latitude will achieve larger relative azimuth angular variation.

B. Analysis of the Observation Angular Differences Between Adjacent Temporal Samplings

Fig. 10 presents the differences of the viewing zenith angle [$\Delta\theta$; Fig. 10 (a)], the relative azimuth angle [$\Delta\varphi$; Fig. 10 (b)], and the solar zenith angle [$\Delta\theta_0$; Fig. 10(c)] over the temporal sampling interval of 1 h.
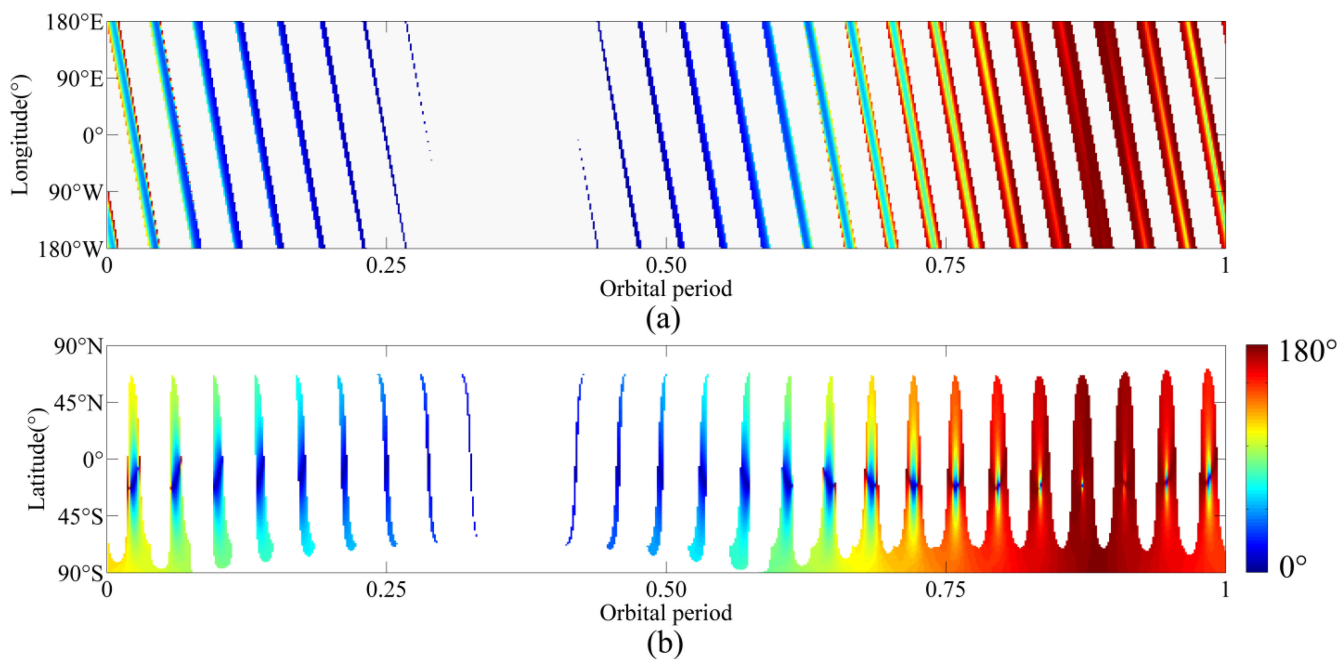
Fig. 9. Relative azimuth angular variation along (a) longitudinal direction and (b) latitudinal direction during one orbital period.
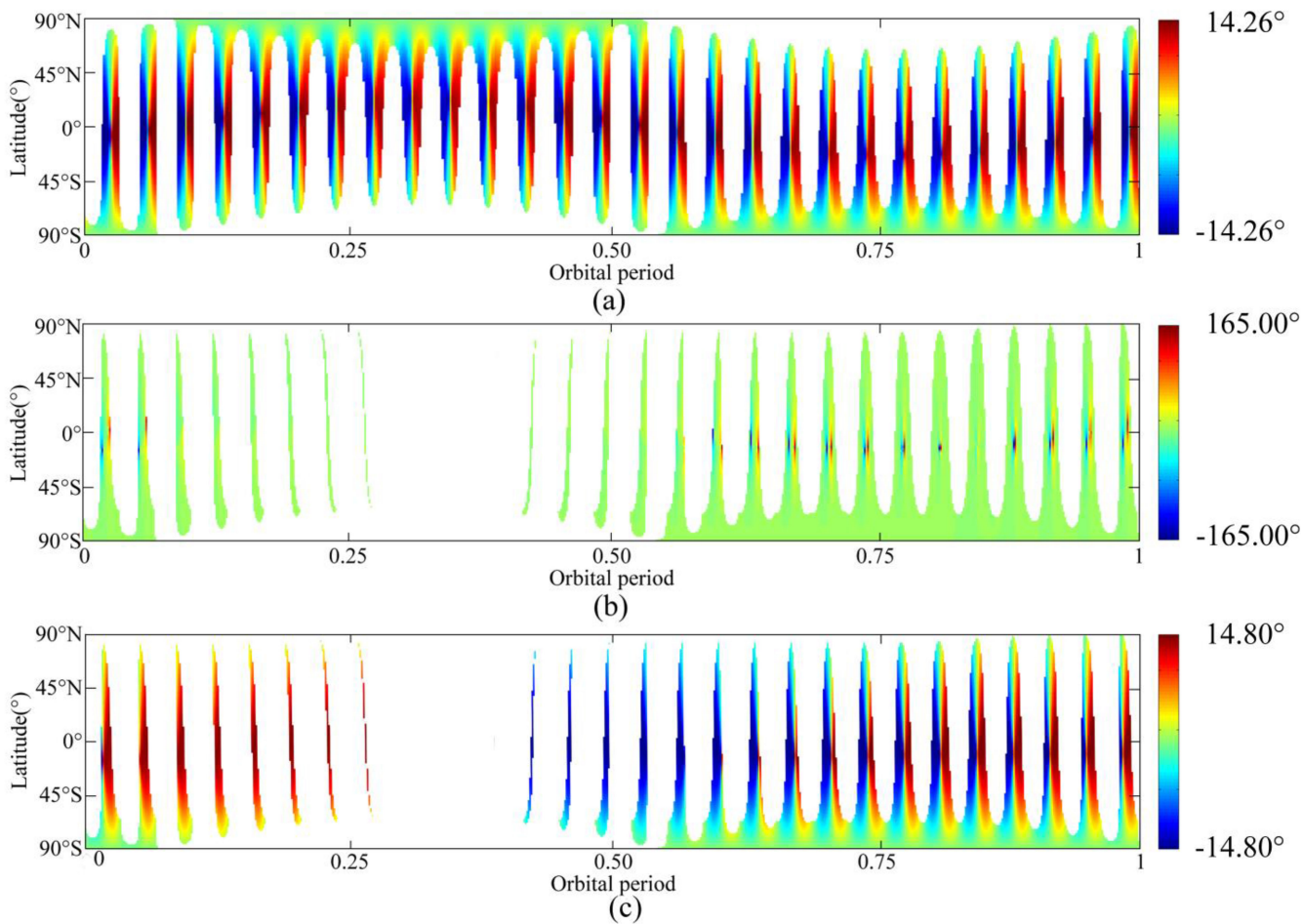

Fig. 10. Differences of (a) viewing zenith angle ($\Delta\theta$), (b) relative azimuth angle ($\Delta\varphi$), and (c) solar zenith angle ($\Delta\theta_0$) over the temporal sampling interval of 1 h during one orbital period.

For the case of the viewing zenith angle, it is illustrated that $\Delta\theta$ shows the periodic variations during one orbital period and the cycle is approximately one day, corresponding to the time the nadir point of the moon-based platform takes around the earth. The pattern of each daily variation is almost the same, but with the changed latitude of the nadir point. $\Delta\theta$ at high latitude region is far smaller than that in the mid-low latitude region. Besides, there is a conspicuous variation of the maximum $\Delta\theta$ lies along the track of the latitude of the nadir point, indicating that the maximum $\Delta\theta$ of the observed points occurs in the nadir point. By analyzing $\Delta\theta$, the characteristics of viewing zenith angle observed from a moon-based platform can be shown, i.e., rapid viewing zenith angular differences, but short observation duration for the observed points at mid-low latitudes, whereas slow angular differences and long-term observations for the observed points at high latitudes.

For the case of the relative azimuth angle, the variation range of $\Delta\varphi$ is relatively large, reaching to 160°. This is because that $\Delta\varphi$ is subjected to both subsolar point and nadir point of the moon-based platform, and closer to these two points, larger values of $\Delta\varphi$ will be shown. Large values mainly occur in the mid-low latitude regions, whereas at the rest regions, $\Delta\varphi$ is small that under 10°. In general, as the only parameter to describe the moon-based platform and the Sun relative to the observed point, the variation of the relative azimuth angle is very important. Fig. 10(b) shows the variations for the observed points at mid-low latitudes are large, thus it is necessary to consider the variation of $\Delta\varphi$ when evaluating the temporal sampling interval of the moon-based earth observations.

The variation of solar zenith angle at different latitude is similar to the case of the viewing zenith angle, and the magnitude of the variation are broadly similar. The difference is that, the illuminated earth disk cannot all the time. Under this circumstance, the daily variations for an observed point will be different during one orbital period. The continuously changing solar zenith angle can benefit the retrieval of the earth's parameters.

C. Effects of Different Temporal Sampling Intervals on the Observation Angles

Different temporal sampling intervals certainly affect the observation angles. To better illustrate the effects of the temporal sampling intervals, Fig. 11 presents the observation angles of the observed point (0°N, 0°E) over the sampling intervals of 1 min [see Fig. 11(a)], 10 min [see Fig. 11(b)], 20 min [see Fig. 11(c)], and 30 min [see Fig. 11 (d)]. It is illustrated that the distribution of these three angles almost covers all the ranges of the viewing zenith angle and relative azimuth angle. From Fig. 11(a)–(d), these three observation angles become sparse with the increment of sampling interval until it loses the distribution characteristics.

To evaluate the effects of the temporal sampling interval on these three observation angles, the maximum values of $\Delta\theta$, $\Delta\varphi$, and $\Delta\theta_0$ at different latitudes with the changing temporal sampling intervals are shown in Fig. 12(a)–(c), respectively. The maximum values of $\Delta\theta$ and $\Delta\theta_0$ have a significant linear correlation with the increasing temporal sampling interval. For
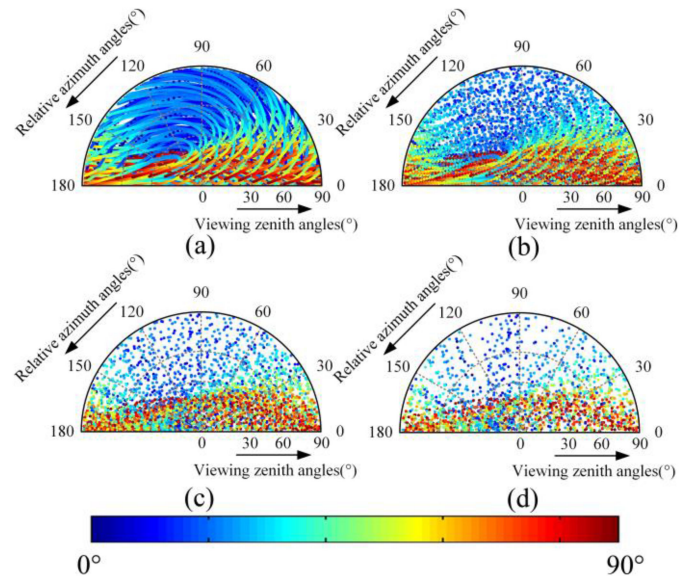

Fig. 11.   Observation angular distribution at the sampling interval of (a) 1 min, (b) 10 min, (c) 20 min, and (d) 30 min.

the case of $\Delta\theta$, the maximum value during one orbital period at a given temporal sampling interval is symmetric with the earth's equator, indicating the uniform samplings of the moon-based earth observations. For the case of $\Delta\theta_0$, since one orbital period is not corresponding to the period the obliquity of the moon path, the maximum value of the solar zenith angle at different latitudes is not symmetric with the earth's equator. As for the case of $\Delta\varphi$, the effects of the temporal sampling interval are not the same. There is a rapid increase for $\Delta\varphi$ of the observed points at 0° and 30°S when the temporal sampling interval is larger than 15 min. That means, enlarging the temporal sampling interval of moon-based earth observations will lead to more loss of the relative azimuth angle at the mid-low latitude regions.

As can be inferred from the results, the observation angles including the solar zenith angle, viewing zenith angle, and relative azimuth angle can describe the current observation of the observed point viewed by a moon-based platform's sensor. Furthermore, different temporal sampling intervals will have different impacts on the observation angles of the points at different latitudes, mainly having significant effects on the relative azimuth angle at mid-low latitude regions. In the implementation of the moon-based earth observations, the temporal sampling interval selection is an extraordinarily significant issue. The temporal sampling interval selection strategy is primarily centered on the scientific goals. For the earth's plasmasphere monitoring, the temporal sampling interval mainly considered the plasmaspheric structures [40]. For the earth's outgoing radiation monitoring, the temporal sampling interval is set to minimize the redundant sampling as much as possible, while at the same time considering the uncertainties and bias [41]. These two scientific goals have a common feature, that is, the requirement of integral observations. The temporal sampling interval selection of these two scientific goals will not consider
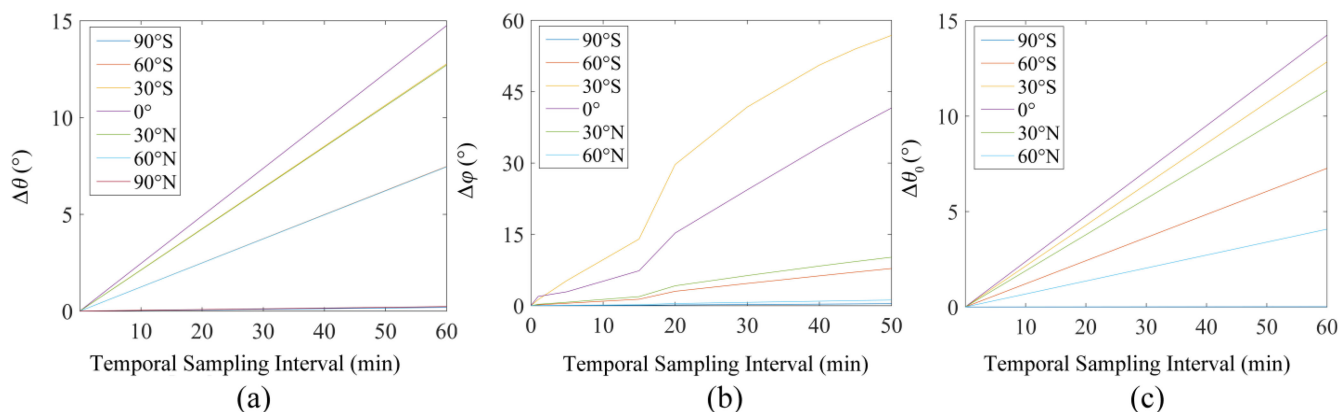
Fig. 12.   Maximum values of (a) $\Delta\theta$, (b) $\Delta\varphi$, and (c) $\Delta\theta_0$ at different latitudes with the changing temporal sampling intervals.

the specific observed points on earth. Actually, compared to the previous studies, the analysis of the effects of the temporal sampling interval starting from the observation geometry is a more fundamental way to understand the moon-based earth observations. It can evaluate the observation geometric variation of the specific observed points in the observation scope with respect to the temporal sampling interval. Thanks to the analysis of this study, enlarging the temporal sampling interval larger will result in significant impacts on the observations of the mid-low latitude regions, especially the regions near the moon-based platform's nadir point and subsolar point.

VI. Conclusion

This study investigated the effects of the temporal sampling interval on the moon-based earth observation geometry. Three observation angles are used to characterize the moon-based earth observation geometry, namely the viewing zenith angle, solar zenith angle, and the relative azimuth angle. Then, theoretical model for the observation angles is proposed. Since the moon is a celestial body, the effects of different positions at lunar surface on the observation angles are analyzed. Based on the variation characteristics of these three observation angles, the effects of the temporal sampling interval on the observation angles are revealed.

It is found that the observation angles can reflect the moon-based earth observation geometry. The nadir point and subsolar point are dominating factors in determining the variation of the solar zenith angle and the viewing zenith angle respectively, whereas the variations of the relative azimuth angle are subject to the relative motion of the moon-based platform's nadir point and the subsolar point. Different temporal sampling intervals will have different impacts on the observation angles. Specifically, the effects of the temporal sampling intervals are profoundly significant to affect the sampling of the relative azimuth angle at mid-low latitude regions. In conclusion, for the moon-based earth observations, the coarser temporal sampling interval will lead to larger variations of the observation geometry at mid-low latitude regions, which is mainly reflected on the loss of the relative azimuth angle.

References

[1] A. F. Chicarro, "Mission to the moon: An ESA study on future exploration," in *Proc. 24th Lunar Planet. Sci. Conf.*, 1993, pp. 281–282.

[2] W. Grandl, "Building the first lunar base—Construction, Transport, Assembly," in *Moon: Prospective Energy and Material Resources*, V. Badescu, Ed. Berlin, Germany: Springer, 2012, pp. 633–640.

[3] A. E. Potter and T. L. Wilson, "Physics and astrophysics from a lunar base: First NASA workshop, Stanford, CA, 1989," in *Proc. 1st NASA Workshop*, 1990, Paper 8905272.

[4] S. Zielinski, "NASA's plans for moon base," *Eos Trans. Amer. Geophys. Union*, vol. 87, no. 52, pp. 594–594, 2013.

[5] H. Guo, G. Liu, and Y. Ding, "Moon-based earth observation: Scientific concept and potential applications," *Int. J. Digit. Earth*, vol. 11, no. 6, pp. 546–557, 2018.

[6] G. R. Carruthers and T. Page, "Apollo 16 far ultraviolet imagery of the polar auroras, tropical airglow belts, and general airglow," *J. Geophys. Res.*, vol. 81, no. 4, pp. 483–496, 1976.

[7] G. R. Carruthers and T. Page, "Apollo 16 far-ultraviolet camera/spectrograph: Earth observations," *Science*, vol. 177, no. 4051, pp. 788–791, 1972.

[8] J. R. Johnson, P. G. Lucey, T. C. Stone, and M. I. Staid, "Visible/Near-Infrared remote sensing of earth from the moon," presented at the NASA Advisory Council Workshop Sci. Associated Lunar Exploration Archit., White Papers, 2007. [Online]. Available: http://www.lpi.usra.edu/meetings/LEA/whitepapers/Johnson_etal_v02.pdf

[9] A. Moccia and A. Renga, "Synthetic aperture radar for earth observation from a lunar base: Performance and potential applications," *IEEE Trans. Aerosp. Electron. Syst.*, vol. 46, no. 3, pp. 1034–1051, Jul. 2010.

[10] G. Fornaro, G. Franceschetti, F. Lombardini, A. Mori, and M. Calamia, "Potentials and limitations of moon-borne SAR imaging," *IEEE Trans. Geosci. Remote Sens.*, vol. 48, no. 7, pp. 3009–3019, Jul. 2010.

[11] Z. Xu and K.-S. Chen, "Effects of the earth's curvature and lunar revolution on the imaging performance of the moon-based synthetic aperture radar," *IEEE Trans. Geosci. Remote Sens.*, vol. 57, no. 8, pp. 5868–5882, Aug. 2019.

[12] Z. Xu, K. Chen, and G. Zhou, "Zero-Doppler centroid steering for the moon-based synthetic aperture radar: A theoretical analysis," *IEEE Geosci. Remote Sens. Lett.*, vol. 17, no. 7, pp. 1208–1212, Jul. 2020.

[13] Z. Xu, K. Chen, and G. Zhou, "Effects of the earth's irregular rotation on the moon-based synthetic aperture radar imaging," *IEEE Access*, vol. 7, pp. 155014–155027, 2019.

[14] Y. Z. Ren, H. D. Guo, G. Liu, and H. L. Ye, "Simulation study of geometric characteristics and coverage for moon-based earth observation in the electro-optical region," *IEEE J. Sel. Topics Appl. Earth Observ. Remote Sens.*, vol. 10, no. 6, pp. 2431–2440, Jun. 2017.

[15] H. Ye, H. Guo, G. Liu, and Y. Ren, "Observation scope and spatial coverage analysis for earth observation from a moon-based platform," *Int. J. Remote Sens.*, vol. 39, no. 18, pp. 5809–5833, 2018.

[16] H. Ye, H. Guo, G. Liu, and Y. Ren, "Observation duration analysis for earth surface features from a moon-based platform," *Adv. Space Res.*, vol. 62, no. 2, pp. 274–287, 2018.

[17] Y. T. Song, X. Q. Wang, S. S. Bi, J. T. Wu, and S. P. Huang, "Effects of solar radiation, terrestrial radiation and lunar interior heat flow on surface temperature at the nearside of the Moon: Based on numerical calculation and data analysis," *Adv. Space Res.*, vol. 60, no. 5, pp. 938–947, Sep. 2017.

[18] H. Ye, H. Guo, G. Liu, J. Ping, and Q. Guo, "Impacts of platform's position errors on geolocation for a moon-based sensor," *IEEE Geosci. Remote Sens. Lett.*, vol. 17, no. 1, pp. 112–116, Sep. 2017.

[19] J. Dong *et al.*, "An analysis of spatiotemporal baseline and effective spatial coverage for lunar-based SAR repeat-track interferometry," *IEEE J. Sel. Topics Appl. Earth Observ. Remote Sens.*, vol. 12, no. 9, pp. 3458–3469, Sep. 2019.

[20] H. L. Ye, H. D. Guo, G. Liu, Q. Guo, and J. Huang, "Looking vector direction analysis for the moon-based earth observation optical sensor," *IEEE J. Sel. Topics Appl. Earth Observ. Remote Sens.*, vol. 11, no. 11, pp. 4488–4499, Nov. 2018.

[21] H. D. Guo, H. L. Ye, G. Liu, C. Dou, and J. Huang, "Error analysis of exterior orientation elements on geolocation for a Moon-based Earth observation optical sensor," *Int. J. Digit. Earth*, vol. 13, no. 3, pp. 374–392, 2020.

[22] J. Bak, J. H. Kim, R. J. D. Spurr, X. Liu, and M. J. Newchurch, "Sensitivity study of ozone retrieval from UV measurements on geostationary platforms," *Remote Sens. Environ.*, vol. 118, pp. 309–319, 2012.

[23] M. Antón *et al.*, "Total ozone column derived from GOME and SCIA-MACHY using KNMI retrieval algorithms: Validation against Brewer measurements at the Iberian Peninsula," *J. Geophys. Rese. Atmospheres*, vol. 116, no. D22, 2011, Art. no. D22303.

[24] A. Mannino, M. G. Novak, S. B. Hooker, K. Hyde, and D. Aurin, "Algorithm development and validation of CDOM properties for estuarine and continental shelf waters along the northeastern U.S. coast," *Remote Sens. Environ.*, vol. 152, pp. 576–602, 2014.

[25] R. Niclos, C. Dona, E. Valor, and M. Bisquert, "Thermal-Infrared Spectral and Angular Characterization of Crude Oil and Seawater Emissivities for Oil Slick Identification," *IEEE Trans. Geosc. Remote Sens.*, vol. 52, no. 9, pp. 5387–5395, Sep. 2014.

[26] N. G. Loeb, F. Parol, J.-C. Buriez, and C. Vanbauce, "Top-of-atmosphere albedo estimation from angular distribution models using scene identification from satellite cloud property retrievals," *J. Climate*, vol. 13, no. 7, pp. 1269–1285, 2000.

[27] N. G. Loeb, B. A. Wielicki, D. R. Doelling, G. L. Smith, and T. Wong, "Toward optimal closure of the earth's top-of-atmosphere radiation budget," *J. Climate*, vol. 22, no. 3, pp. 748–766, 2009.

[28] H. Guo, Y. Ren, G. Liu, and H. Ye, "The angular characteristics of moon-based earth observations," *Int. J. Digit. Earth*, vol. 13, no. 3, pp. 339–354, 2020.

[29] E. Pallé and P. R. Goode, "The Lunar Terrestrial Observatory: Observing the earth using photometers on the moon's surface," *Adv. Space Res.*, vol. 43, no. 7, pp. 1083–1089, 2009.

[30] W. M. Folkner, J. G. Williams, and D. H. Boggs, "The Planetary and Lunar Ephemeris DE 421," Interplanetary Netw. Prog. Rep., IPN Prog. Rep. 42–178, 2009.

[31] A. Fienga, H. Manche, J. Laskar, and M. Gastineau, "INPOP06: A new numerical planetary ephemeris," *Astron. Astrophys.*, vol. 477, no. 1, pp. 315–327, 2008.

[32] E. V. Pitjeva, "EPM ephemerides and relativity," *Proc. Int. Astron. Union*, vol. 5, no. 261, pp. 170–178, 2010.

[33] W. M. Folkner, J. G. Williams, D. H. Boggs, R. S. Park, and P. Kuchynka, "The planetary and lunar ephemerides DE430 and DE431," Interplanetary Netw. Prog. Rep., IPN Prog. Rep. 42-196, 2014.

[34] G. Petit, B. Luzum, and E. Al, "IERS conventions," *IERS Techn. Note*, vol. 36, pp. 1–95, 2010.

[35] O. Montenbruck and E. Gill, "Satellite orbits, models, methods and applications," *Appl. Mech. Rev.*, vol. 55, no. 2, pp. 170–188, 2002.

[36] P. K. Seidelmann *et al.*, "Report of the IAU/IAG Working Group on cartographic coordinates and rotational elements: 2006," *Celestial Mech. Dyn. Astron.*, vol. 98, no. 3, pp. 155–180, 2007.

[37] GSFC, "A standardized lunar coordinate system for the lunar reconnaissance orbiter and lunar datasets," LRO Project LGCWG White Paper Version 5, Goddard Space Flight Center, Greenbelt, MD, USA, 2008.

[38] P. K. Seidelmann, "1980 IAU Theory of Nutation: The final report of the IAU Working Group on Nutation," *Celestial Mech. Dyn. Astron.*, vol. 27, no. 1, pp. 79–106, 1982.

[39] C. A. Murray and J. Kovalevsky, "Book-Review - Vectorial Astrometry," *Space Sci. Rev.*, vol. 37, no. 3, p. 400, 1984.

[40] F. He, X. X. Zhang, B. Chen, M. C. Fok, and Y. L. Zou, "Moon-based EUV imaging of the earth's plasmasphere: Model simulations," *J. Geophys. Res.—Space Phys.*, vol. 118, no. 11, pp. 7085–7103, Nov. 2013.

[41] H. Ye, H. Guo, G. Liu, Q. Guo, L. Zhang, and J. Huang, "Temporal sampling error analysis of the earth's outgoing radiation from a moon-based platform," *Int. J. Remote Sens.*, vol. 40, no. 18, pp. 6975–6992, 2019.
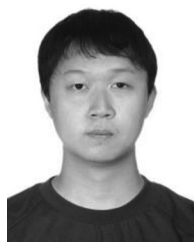
Hanlin Ye received the Ph.D. degree in cartography and geographical information system from the University of Chinese Academy of Sciences, Beijing, China, in 2019.

Since 2015, he has been in part of the major program of National Natural Science Foundation of China "Moon-based observation research of earth macroscopic scientific phenomena." He has authored or coauthored nine peer-reviewed journal articles related to the topic of moon-based earth observations. His general interests include the earth's outgoing radiation monitoring and the moon-based earth observation conceptual studies, particularly the potential applications in the field of earth's outgoing radiation monitoring.

Wei Zheng received the Ph.D. degree in physics from the College of Physics, the Huazhong University of Science and Technology, Wuhan, China, in 2007, and the Postdoctoral degree from Kyoto University, Kyoto, Japan, in 2010.

He was with the Institute of Geodesy and Geophysics, Chinese Academy of Sciences, Beijing, China, and is currently a Professor with Qian Xuesen Laboratory of Space Technology, China Academy of Space Technology, Beijing, China. He has more than 70 research papers as the first author (31 papers included in SCI) and more than 30 research papers included in SCI as the corresponding authors and coauthors. In addition, he has four academic monographs in Science Press as an independent/first author. His main research direction is the satellite gravity recovery and the navigation and detection based on the information of aerospace–aeronautics–marine integration. Also, he is doing research on the design of high-orbital satellite and its potential scientific goals.

Huadong Guo (Member, IEEE) received the Graduate degree in geology from the Geology Department, Nanjing University, Nanjing, China, in 1977, and the M.Sc. degree in cartography and geographical information system from the Graduate University of the Chinese Academy of Science (CAS), Beijing, China, in 1981.

He is currently the Academician of the CAS, the Foreign Academician of the Russian Academy of Sciences, the Foreign Academician of the Finland Academy of science and humanities, the Academician of the developing countries Academy of Sciences, and the Academician of the International Academy of Sciences of Eurasia. He is the President of the International Digital Earth Society, the Chairman of the International Environmental Remote Sensing Committee, the member of the Expert Group of the United Nations technical promotion mechanism for Sustainable Development Goals, the Director of the International Centre for Space Technology for Natural and Cultural Heritage of UNESCO, the Editor of *International Journal of Digital Earth* and *International Journal of Big Earth Data*. He was a Project Leader of more than ten key programs related to earth observation and is the Principal Investigator for SIR-C/X-SAR, JERS-1 SAR, ERS-1/2 SAR, Radarsat-1/2, Envisat, SRTM, and ALOS programs. He has authored or coauthored more than 200 SCI index papers and 16 books.

Prof. Guo was the recipient of three national awards on science and technology and nine awards by the CAS.

Guang Liu (Member, IEEE) received the B.S. and M.S. degrees in physics from Tsinghua University, Beijing, China, in 1999 and 2002, respectively, and the Ph.D. degree in cartography and geography information system from the Institute of Remote Sensing Applications, Chinese Academy of Sciences (CAS), Beijing, China, in 2008.

From 2006 to 2007, he visited the Mathematical Geodesy and Positioning, the Delft University of Technology, Delft, The Netherlands, as a Guest Researcher and worked on the time-series analysis of phased array type L-band synthetic aperture radar (PALSAR) data. He is currently a Professor with the Aerospace Information Research Institute, CAS. He is a Principal Investigator of the Key Program of National Natural Science Foundation of China, focused on the frontier research of the Lunar-based earth observation platform. He authored or coauthored more than 30 lead-authored and 35 coauthored peer-reviewed journal articles. His research interest includes the moon-based earth observation conceptual studies, he feasibility and potential applications of InSAR time-series analysis especially in mountain areas, such as glacier change and landslide studies.